Mechanical Behaviour of Dual Phase Steels under Different Strain Rates

*L. Topilla** and *S. Toros*

Nigde Omer Halisdemir University, Mechanical Engineering Department, 51 245, Nigde, Turkey

Abstract
The objective of this research was to analyse the stress and strain behaviours of the triaxiality specimens (specimens of different shaping) of dual-phase steels, respectively DP600 and DP800, whose microstructures mainly comprise ferrite and martensite phases. These steels find wide application in the automotive industry, which is constantly searching for better quality materials in the aim of increasing vehicle safety, protecting the environment, and reducing fuel consumption. In this case, for all tested specimens the experimental uniaxial tensile tests were performed at three different strain rates, 0.0083 s^{-1}, 0.042 s^{-1}, and 0.16 s^{-1}, to determine mechanical properties such as stress, strain, yield strength, and ultimate tensile strength of mentioned steels. In addition, uniaxial tensile tests with characteristics similar to those experimental were carried out through the finite element modelling method using the Mat_Picewise_Linear_Plasticity_024 model, to determine the mentioned mechanical properties, but also to determine the failure parameters or plastic strain up to failure, of all triaxiality modelled specimens. The obtained results were validated by comparing the experimental results with numerical simulation results. The comparative scale of accuracy between both steels was made at the fracture strain, and the average accuracy of both steels for the standard (s) specimens was < 1 %, for the (20a) specimens 1.50 %, for the (4a) specimens 4 %, and for (a) specimens 3.50 %. Finally, it was concluded that the proposed material model and calibrated failure data fitted very well.

Keywords
Triaxiality, dual phase steel, numerical simulations, strain rate, failure limit

1 Introduction

Dual phase steels, (DP), are a new generation of high-strength steel families, which were developed in the late 1970s, and are characterised by microstructure consisting of ferrite and martensite phases.[1–6] Since these materials can meet criteria such as strength and formability, they are particularly preferred in the automotive industry.[7–9] There are two types of DP steels that can be produced in general: hot rolling dual phase steels (HRDP), and cold rolling dual phase steels (CRDP). The advantages of hot rolling and cold rolling were also demonstrated in the description of the structure and microstructure of DP steels. Thus, a DP structure develops during cooling after hot rolling in the first example, while a DP structure develops after intercritical annealing of a previously rolled product in the second case. Cooling within a suitable speed range allows some austenite to convert to ferrite and some to martensite in both circumstances.[10] On the other hand, to produce the DP structure in these materials, cold-rolled steels are typically intercritically annealed on a hot-dip galvanizing line. Although martensite plays an essential role in the mechanical characteristics of ferrite-martensite-DP steels, according to the researchers, the crystallography and microstructure of lath martensite in DP-steels has not been studied in depth.[11] Furthermore, the tensile and impact strengths of the developed DP steels increased with intercritical annealing (ICA) temperatures, with optimal properties achieved at 790 °C, owing to the finer microstructure of the phase components and the absence of carbide deposits, which allows for a slight dislocation flow.[12] On the other hand, the effect of temperature on the mechanical properties and fracture behaviours of DP1000 steel, were used to investigate the variations in mechanical properties, by carrying out uniaxial tensile tests in various rolling directions (RD).[13–14]

Nowadays, a variety of experimental techniques have been developed by engineers to mechanically test engineering materials exposed to stress, compression, bending, or torsion loading. The most popular type of test used to determine the mechanical properties of materials is the tension test. The purpose of conducting the tension test is to provide basic material strength design data. Tension verification is also referred to as an approved test for the quality of materials.[15] Therefore, one of the most fundamental tests for engineering is the tensile test, which provides valuable information about a material and its properties. These properties can be used for the planning and analysis of construction structures, as well as for the development of new materials that are best suited for a specific use. However, the tensile test is a mechanical test in which an attractive force is exerted on both or one side of the material until the sample changes shape or breaks down. It is a general and important test that provides a variety of information about the material being tested, including elongation, yield strength, tensile strength, and tensile failure.[16–18] Due to their good mechanical qualities, dual phase steels are finding a wide range of applications in the automotive engineering sectors, and can be subjected to forming/stamping processes.[19–23]

In addition to experimental testing, there are now many different softwares, where different hardening or failure parameters can be defined by different models. Moreover,

* Corresponding author: Labinot Topilla, PhD
  Email: labinot.topilla@gmail.com

Table 1 – Chemical composition of DP600, and DP800 steels (wt-%)

Steel / ng	P	Si	Cu	Ni	Cr	Mn	C – Ferrite	C – Martensite
DP800	0.015	0.230	0.050	0.030	0.020	1.420	0.006	0.294
DP600	0.015	0.100	0.000	0.000	0.480	1.580	0.006	0.234

(Generalized Incremental Stress-State Dependent Damage Model), GISSMO, is used to describe the evolution of ductile damage and to predict the onset of fracture.[24] Based on physical features of the microstructure, a hybrid composite medium-field (Hy-MFC) model was developed to predict the tensile properties of dual-phase steels under monotonic loading.[25]

While considering the studies in the literature, it was observed that the mechanical properties of some DP steels have been investigated by other models,[26–33] and that is no study on triaxiality and strain rate behaviour of the DP600 and DP800 using specifically the Mat_Picewise_Linear_Plasticity_024 model, which is found in LS-Dyna software, from where an elasto-plastic material with an arbitrary stress versus strain curve and arbitrary strain rate dependency can be defined. In addition, it can be defined that failure is based on plastic strain. Therefore, the purpose and the novelty part of this research was to define failure parameters (FAIL) for triaxiality specimens of DP600 and DP800 steels, and to predict effective plastic strain at fracture at three different strain rates. Thus, failure parameters are plastic strains up to failure or when the plastic strain reaches this value, the element is deleted from the FE calculation.

2 Experimental methodologies

Based on the positive properties that DP steels possess, efforts were made to do more in-depth or specific research to better understand the stress and strain behaviours of DP600 and DP800 steels by performing the uniaxial tensile test at three various strain rates. All tests were carried out in laboratory conditions at room temperature on a Shimadzu Autograph 100 kN testing machine equipped with a data gathering system controlled by a digital interface board and a specific computer program. A video-extensometer measurement device was used to measure material deformation similar to.[34] Therefore, the specimens were of different geometric shapes based on the standard ASTM E8 (see Fig. 1), and cut at 0° degree of (RD). The geometrical measurements of the specimens were made with special focus on their thickness, which was 0.78 mm, width was 12.5 mm, and gauge length was 50 mm. All specimens were designated as: standard (s), 20a, 4a, and a. Finally, after performing the uniaxial tensile tests, all the results were collected as such and presented as engineering stress-strain, true stress-strain, or effective plastic strain Hollomon's power law. These results are very significant for the realisation of simulations, and for comparing the final results.

2.1 Chemical Composition of DP600, DP800, and DP1000

The chemical compositions of the DP600, DP800, steels are listed in Table 1, where P is present in a similar percentage in two steels; Si is found in a higher percentage in DP800 with a value of 0.23 % compared to 0.1 % found in both DP600; 0.05 % of Cu is detected in DP800; 0.02 % of Cr is found in DP800 compared to 0.48 % in DP600, and Mn is proportionally distributed in two steels. Regarding the stress-strain curves of the steels, % C had the highest impact on strengthening. The percentage of carbon in these two steels was measured at the level of both ferrite and martensite phases.

2.2 Mathematical formulas and equations

Following the completion of the experimental testing, the necessary calculations were completed to realise the experimental and simulation processes, as well as the option of comparing the outcomes. Engineering stress-strain, true stress-strains, and hardening curves were primarily used in computations. Engineering and true stress-strains were carried out based on general principles, Eq. (1)–(4):

$$\sigma_{\text{eng}} = \frac{F}{A_0} \tag{1}$$

$$\varepsilon_{\text{eng}} = \frac{l - l_0}{l_0} = \frac{\Delta l}{l_0} \tag{2}$$

$$\varepsilon_{\text{true}} = \ln\left(1 + \sigma_{\text{eng}}\right) \tag{3}$$

$$\sigma_{\text{true}} = \sigma_{\text{eng}}\left(1 + \sigma_{\text{eng}}\right) \tag{4}$$

where σ_{eng} is the engineering stress, ε_{eng} is the engineering strain, F is the external axial tensile load, A_0 is the original cross-sectional area of specimen, l_0 is the original length of specimen, and l is the final length of specimen. Whereas, $\varepsilon_{\text{true}}$ is true strain, σ_{true} is true stress. The yield strength is often defined as the stress at which the plastic strain is 2 % (Eq. (5)):

$$\sigma_{\text{y}} = \frac{F_{\text{y}}}{A_0} \tag{5}$$

The intersection of a line parallel to the elastic portion of the curve and the stress-strain curve yields this result. The stress-strain curve will reach its highest point, which is the ultimate tensile strength when continuous loading is applied (σ_{UTS}) (Eq. (6)):

$$\sigma_{UTS} = \frac{F_{max}}{A_0} \quad (6)$$

The specimen may be under the most stress at this point before necking. This is seen as a local reduction in the cross-sectional area of the specimen, which usually appears at the gauge length's center.[35] Equivalent strain at fracture strength, is defined as the fracture strain (Eq. (7)):

$$\varepsilon_{fracture} = \frac{F_{fracture}}{A_0} \quad (7)$$

The fracture strain of the specimen can be calculated by drawing a straight line parallel to the slope in the linear relationship starting at the fracture point of the stress-strain curve. The interception of the parallel line at the x axis indicates the fracture strain.[15] True plastic curve can be approximated by a power-law expression Eq. (8):

$$\sigma = K\varepsilon^n \quad (8)$$

Here σ can be interpreted as the new yield strength after a cold reduction, and K is the hardening strength coefficient. Because the tensile true stress, σ, and true tensile strain, ε, in a tension test are the effective stress and strain.[13] The triaxiality values formed in the material for the samples in Fig. 1 can be calculated from Eq. (12).

$$\eta = \frac{1}{3} + \ln\left(1 + \frac{a}{2R}\right) \quad (9)$$

Equality is the depth of the notch, and R can be defined as the notch width, which varies according to this value. These values apply to the first value of the load condition of the material and can change with the deformation. This value remains constant only for flat samples without a notch and the triaxiality values for the tensile tested specimens are presented by η (see values in Table 2). Triaxiality specimens tested and their stress-strain resulting curve for each as well as for all of them together are shown in Fig. 1.

2.3 Finite element modelling method

During this research, the model Mat_Picewise_Linear_Plasticity_024 was used. This model was integrated into LS-DYNA software, from where it was possible to define an elasto-plastic material with arbitrary stress versus strain curve and strain rate dependency. Additionally, failure based on a plastic strain or a minimum time step size could be defined. The solid element was used during the construction of triaxiality specimen key cards, to perform numerical simulations. All the properties of the mechanical data placed on the key cards were similar to the experimental data, including similarity to geometric shapes of specimens, their size, thickness, width, time duration, and strain rate applied to perform uniaxial tensile testing. In both specimen key cards for DP600 and DP800 steels, mechanical characteristics were also included: density ($p = 7.830 \cdot 10^{-6}$), Young module ($E = 216$), Poisson ratio ($v = 0.28$) as well as yield stress (σ_y). In addition, experimental Hollomon's curves were determined from
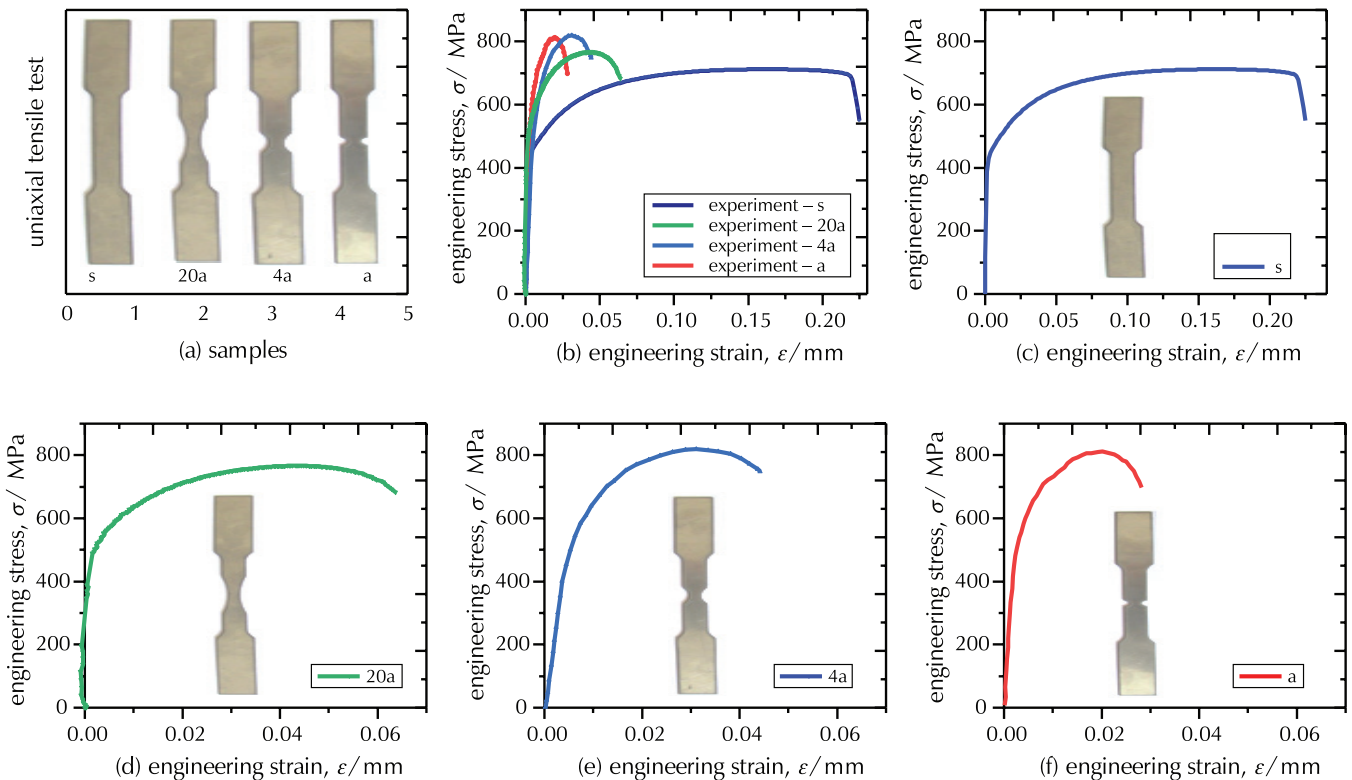

Fig. 1 – Experimental stress-strain relations of triaxiality specimens

the standard samples used, being modified on the basis of materials and on the basis of strain rates, then are placed at Load curve ID (LCSS). Finally, failure parameters (FAIL) were calibrated through rerunning the simulations up to desired results.

3 Results and discussion

The results expressed in Figs. 2–7 and Table 2 show the graphical and tabular comparisons of mechanical results between the experimental and the numerical simulations obtained after calibrated failure parameters. In this case, the used materials were DP600 and DP800 steels, cut at

$0°$ of rolling direction (RD = $0°$). In both cases, the uniaxial tensile test was realised at strain rate of $\varepsilon_r = 0.0083$ s^{-1}, 0.042 s^{-1}, and 0.16 s^{-1}, to determine failure parameters (FAIL) for both steels. In Figs. 2–7(a), comparisons of engineering strain curves σ_{eng} have emerged. In this case, the fitting of the curves are in good agreement, see Figs. 2–3 for DP600 steel, and Figs. 5–6(a) for DP800 steel. In Fig. 4 for DP600 steel, and in Fig. 7 for DP800 steel at specimen 20a, the curve differs from the aforementioned two cases, because the 20a curve obtained by numerical simulation is lower than the curve of the experiments, while the curves belonging to samples s, 4a, and a, also obtained by numerical simulations, are in good agreement, while comparisons for failure value derived from simulations are expressed as effective plastic strain and are shown in Figs. 2–7(b).
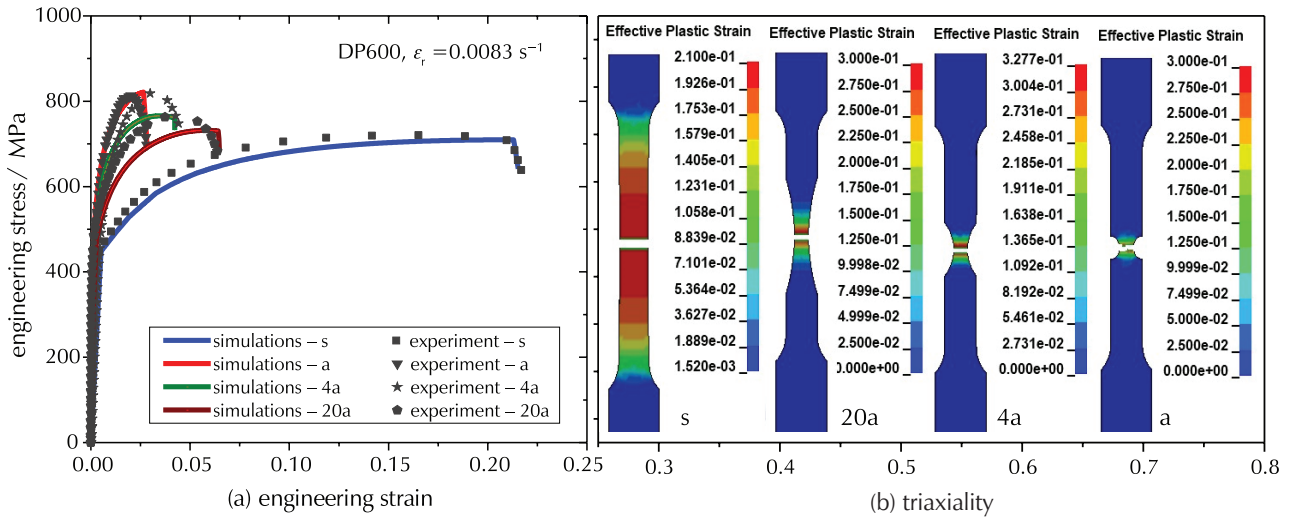

Fig. 2 – Experimental and numerical simulation results of DP600 steel, $\varepsilon_r = 0.0083$ s^{-1}, (a) comparisons of engineering stress-strain curves, (b) predicted effective plastic strain at fracture
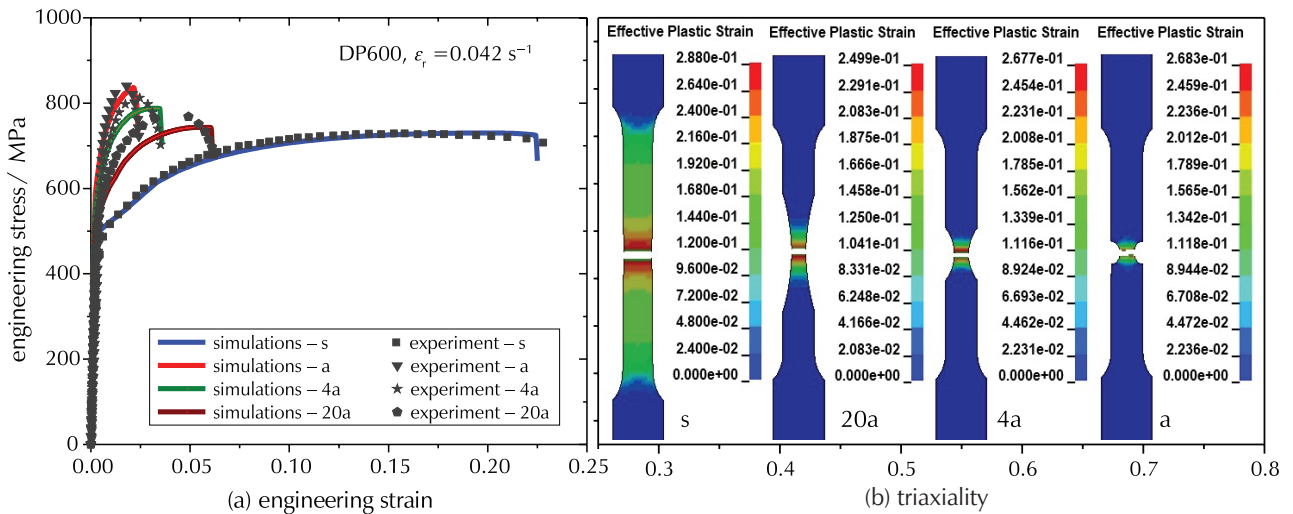

Fig. 3 – Experimental and numerical simulation results of DP600 steel, $\varepsilon_r = 0.042$ s^{-1}, (a) comparison of engineering stress-strain curves, (b) predicted effective plastic strain at fracture

Fig. 4 – Experimental and numerical simulation results of DP600 steel, $\varepsilon_r = 0.16$ s^{-1}, (a) comparison of engineering stress-strain curves, (b) predicted effective plastic strain at fracture
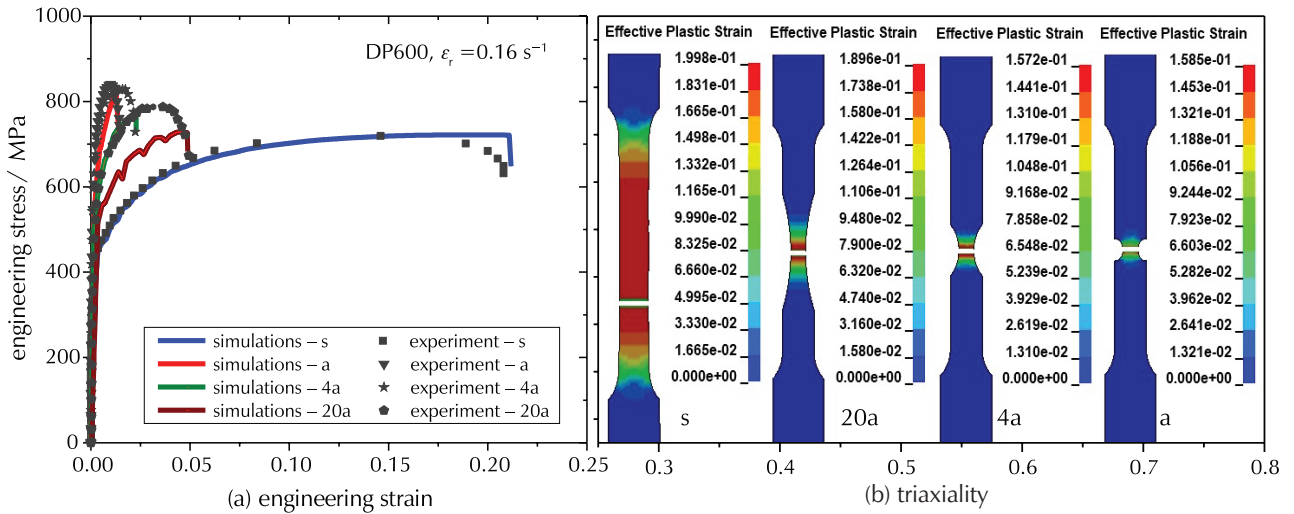

Fig. 5 – Experimental and numerical simulation results of DP800 steel, $\varepsilon_r = 0.0083$ s^{-1}, (a) comparison of engineering stress-strain curves, (b) predicted effective plastic strain at fracture
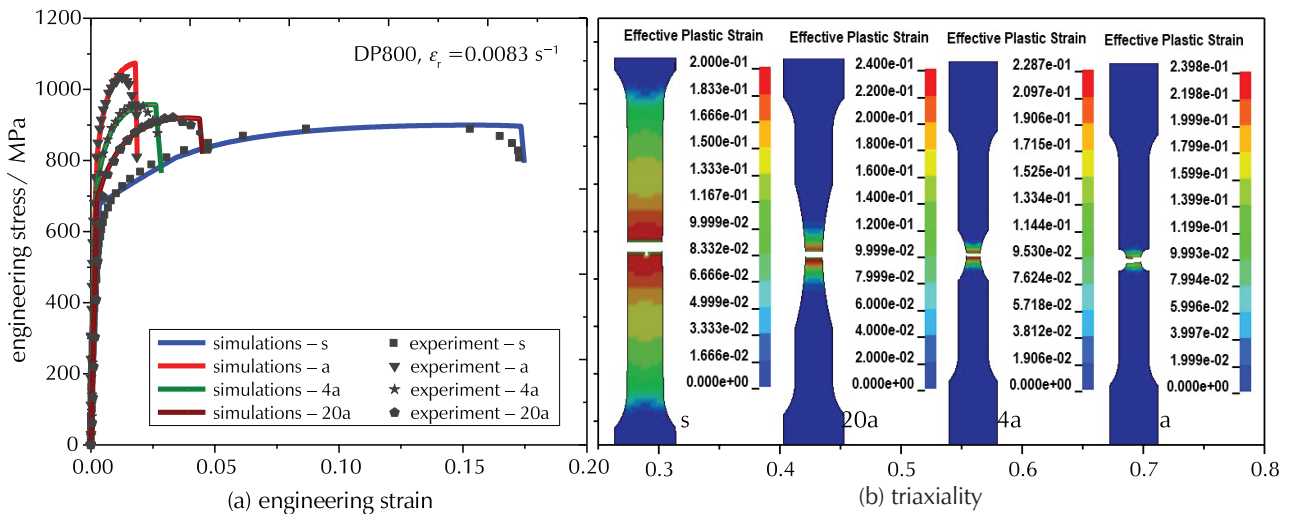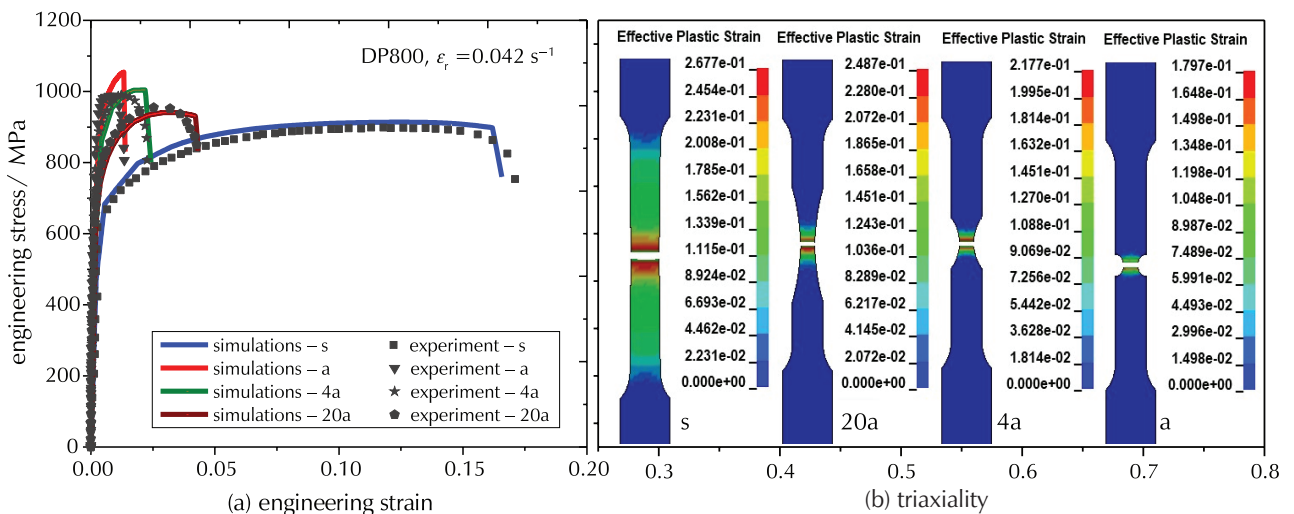

Fig. 6 – Experimental and numerical simulation results of DP800 steel, $\varepsilon_r = 0.042$ s^{-1}, (a) comparison of engineering stress-strain curves, (b) predicted effective plastic strain at fracture
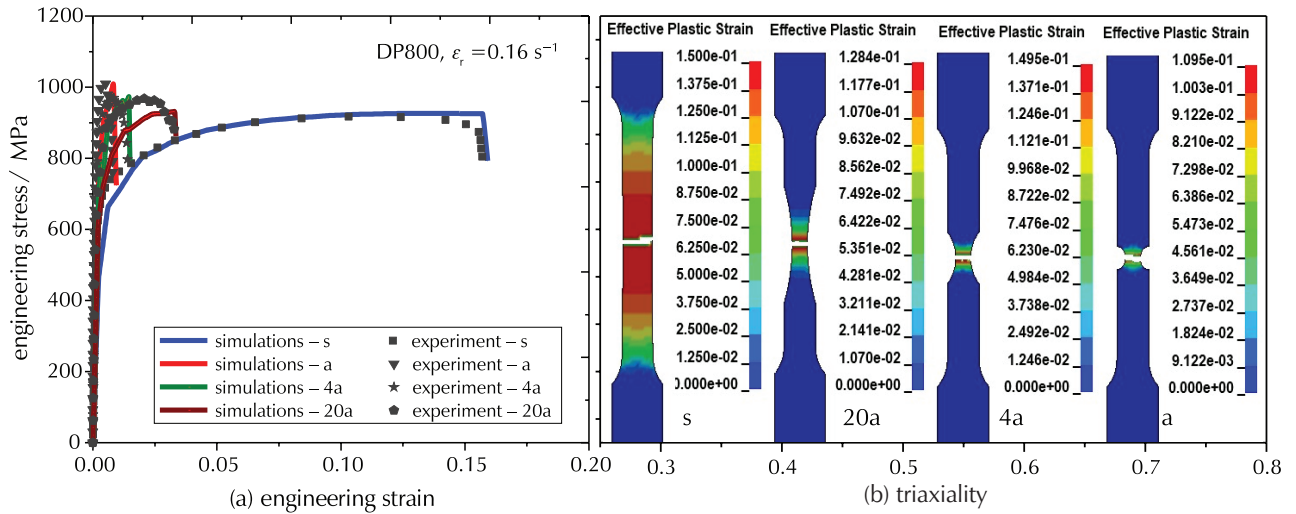
Fig. 7 – Experimental and numerical simulation results of DP800 steel, ε_r = 0.16 s⁻¹, (a) comparison of engineering stress-strain curves, (b) predicted effective plastic strain at fracture

Comparisons of mechanical properties between experimental and numerical simulation results concerning engineering stress-strain properties are summarised in Table 2. Table 2 shows the relative errors (RE) expressed by percentage (%) of both steels. The RE was done for these specific properties included ultimate tensile strength (σ_{UTS}), and engineering fractures strain ($\varepsilon_{engfracture}$). However, even the uniaxial tensile tests were realised at different strain rates, generally all results were in good agreement. Specifically, the most suitable results or RE were for standard (s) specimens of both steels. Meanwhile, at the strain rate of 0.16 s⁻¹, the RE of σ_{UTS} appears to have some noticeable differences in the 20a specimens of both steels. Regardless of the different degrees of strain rate, such RE does not

appear in samples (4a) DP800 and (a) DP600 and DP800, except for samples 4a of DP600 steel, where in all three strain rates RE and σ_{UTS} has more pronounced percentage.

3.1 Finite element modelling results and discussion

Within this model, three options based on viscoplastic activations are possible to be accounted for strain rate effects. In this case, the used option was with active viscoplastic option VP = 1.0 and the yield strength (SIGY) is > 0. Then, the dynamic yield stress is computed from the sum of the static stress, which is typically given by a load curve ID, and the initial yield stress, SIGY, multiplied by the Cowper-Symonds rate term as follows, where the plastic strain rate is used.

$$\sigma_y\left(\varepsilon_{eff}^p, \dot{\varepsilon}_{eff}^p\right) = \sigma_y^s\left(\varepsilon_{eff}^p\right) + SIGY \cdot \left(\frac{\dot{\varepsilon}_{eff}^p}{C}\right)^{1/p} \tag{10}$$

where σ_y is the yield strength, ε_{eff} is the effective plastic strain, $\sigma_y^s\left(\varepsilon_{eff}^p\right)$ is the static stress, and C and p are the strain rate parameters.

Therefore, the simulations were carried out in order to determine failure parameters (see Table 3), through which the degree of effective plastic strain under different strain

Table 2 – Comparison between experimental and numerical simulation results

Designation			DP600 steel		DP800 steel	
Specimen, triaxiality			(σ_{UTS}) MPa	($\varepsilon_{engfracture}$)	(σ_{UTS}) MPa	($\varepsilon_{engfracture}$)
	η	Strain rate	RE %	RE %	RE %	RE %
s		0.0083 s⁻¹	−1.69 %	−0.72 %	1.11 %	1.16 %
s	0.33	0.042 s⁻¹	0.27 %	−1.31 %	1.64 %	−3.19 %
s		0.16 s⁻¹	0.42 %	1.77 %	1.08 %	1.39 %
20a		0.0083 s⁻¹	−4.24 %	1.79 %	−0.22 %	−4.60 %
20a	0.36	0.042 s⁻¹	−3.36 %	−1.44 %	1.39 %	6.47 %
20a		0.16 s⁻¹	−8.10 %	−1.48 %	−3.97 %	2.03 %
4a		0.0083 s⁻¹	−6.93 %	−4.56 %	0.52 %	5.32 %
4a	0.45	0.042 s⁻¹	−3.05 %	1.73 %	−1.49 %	1.20 %
4a		0.16 s⁻¹	4.72 %	1.80 %	0.41 %	6.42 %
a		0.0083 s⁻¹	1.10 %	0.63 %	3.45 %	0.96 %
a	0.74	0.042 s⁻¹	−0.48 %	−1.94 %	6.36 %	3.76 %
a		0.16 s⁻¹	−3.07 %	−5.05 %	0.00 %	5.45 %

Table 3 – Failure parameters for numerical simulations (FAIL)

Strain rates /s⁻¹	DP600				DP800			
	s	20a	4a	a	s	20a	4a	a
0.0083	0.21	0.3	0.33	0.3	0.2	0.24	0.23	0.24
0.0420	0.29	0.25	0.27	0.27	0.27	0.25	0.22	0.18
0.166	0.2	0.19	0.16	0.15	0.15	0.15	0.12	0.11

rates was determined for the above materials. The numerical comparisons between triaxiality failure values shown by curves for both steels are presented in Fig. 8 (dash spline DP600 and solid spline DP800).
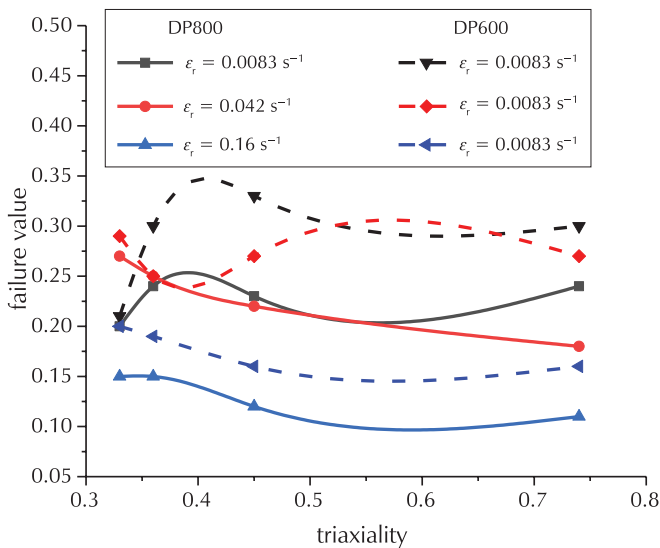

Fig. 8 – Comparison between failure values of the numerical simulation results of triaxiality specimens

4 Conclusion

The uniaxial tensile test was conducted on four different test specimens, made of DP600 steel and DP800 steel, with an approximate thickness of 0.78 mm, and with 12.5 mm, and approximate gauge length $GL = 50$ mm, where the uniaxial tensile test was done respectively at three different strain rates. Based on the results, it was concluded that the strain rate and triaxiality of the specimens had huge effect on the properties of steel materials, mainly on yield strength and ultimate tensile strength, and fracture strain. Nevertheless, the maximum elongations at engineering and true stress values appeared in standard (s) specimens. It is important to note that in s specimens no huge differences at elongations as result of strain rate were noticed. However, the most noticed effect as result of strain rate appeared in specimens 20a, 4a, and a. On the other hand, regarding ultimate tensile strength, there were some significant effects of strain rate that made some difference between specimens. Therefore, appropriate stress and strain relations of the designated specimens should be defined through finite element modelling. The failure value differs from one specimen to another. The differences appear to be at different strain rates also. Through these simulations, adequate failure values were determined for all the mentioned species. Future research should publish fracture failure parameters for named steels even at the microstructure level through Gurson and Johnson-Cook models.

List of abbreviations and symbols

DP   – dual phase

HRDP   – hot rolling dual phase

CRDP   – cold rolling dual phase

ICA   – intercritical annealing

LCSS   – load curve ID

FAIL   – failure parameters

σ_{eng} – engineering stress

ε_{eng} – engineering strain

ε_{eff} – effective plastic strain

F – external axial tensile load

A_0 – original cross-sectional area

l_0 – original length of the specimen

l – final length

σ_{true} – true stress

ε_{true} – true strain

σ_Y – yield strength

σ_{UTS} – ultimate tensile strength

$\varepsilon_{engfracture}$ – engineering fractures strain

ε_r – strain rate

ε_f – fracture strain

K – hardening strength coefficient

n – hardening strength exponent

η – triaxiality

p – density

E – Young module

v – Poisson ratio

References
Literatura

1. *M. Kulakov, W. J. Poole, M. Militzer*, A microstructure evolution model for intercritical annealing of a low carbon dual phase steel, ISIJ Int. **54** (11) (2014) 2627–2636, doi: https://doi.org/10.2355/isijinternational.54.2627.

2. *C. M. Gómora, R. R. Ambriz, C. J. García, I. Ruíz-López, D. Jaramillo*, Dissimilar Dual Phase-Low Carbon Steel Joints by the GMAW Process Subjected to Impact Load, Metals (Basel). **12** (3) (2022) 404, doi: https://doi.org/10.3390/met12030404.

3. *T. Robl, C. Krempaszky, A. Fillafer, E. Werner*, Examining the unloading behavior of dual-phase steels by means of microstructure simulations, Mater. Sci. Eng. **823** (2021) 141744, doi: https://doi.org/10.1016/j.msea.2021.141744.

4. *S. Katani, S. Ziaei-Rad, N. Nouri, N. Saeidi, J. Kadkhodapour, N. Torabian*, Microstructure Modelling of Dual-Phase Steel Using SEM Micrographs and Voronoi Polycrystal Models, Metallogr. Microstruct. Anal. **2** (3) (2013) 156–169, doi: https://doi.org/10.1007/s13632-013-0075-7.

5. *K. Park, M. Nishiyama, N. Nakada, T. Tsuchiyama, S. Takaki*, Effect of the martensite distribution on the strain hardening and ductile fracture behaviors in dual-phase steel, Mater. Sci. Eng. **604** (2014) 135–141, doi: https://doi.org/10.1016/j.msea.2014.02.058.

6. *O. Çavuşoğlu, S. Toros, H. Gürün*, Microstructure based modelling of stress–strain relationship on dual phase steels, Ironmak. Steelmak. **46** (4) (2019) 313–319, doi: https://doi.org/10.1080/03019233.2017.1371959.

7. *T. Rahmaan, C. Butcher, A. Abedini, M. Worswick*, Effect of strain rate on shear properties and fracture characteristics of DP600 and AA5182-O sheet metal alloys, EPJ Web of Conferences **94** (2015) 01033, doi: https://doi.org/10.1051/epjconf/20159401033.

8. *D. Anderson, C. Butcher, N. Pathak, M. J. Worswick,* Failure parameter identification and validation for a dual-phase 780 steel sheet, Int. J. Solids Struct. **124** (2017) 89–107, doi: https://doi.org/10.1016/j.ijsolstr.2017.06.018.

9. *S. Ren, N. Ma, S. Tsutsumi, G. Watanabe, H. He, C. Cao*, Post-weld cold working for fatigue strength improvement of resistance spot welded joint of advanced high-strength steel, J. Mater. Process. Technol. **299** (2021) 117364, doi: https://doi.org/10.1016/j.jmatprotec.2021.117364.

10. *B. Carlsson, J. Larsson, T. Nilsson,* Dual Phase Steels for Auto Body: Design, Forming and Welding Aspects, corpus ID: 201742595, url: https://www.phase-trans.msm.cam.ac.uk/2005/LINK/64.pdf.

11. *H. Yoshida, S. Takagi, S. Sakai, S. Morito, T. Ohba*, Crystallographic analysis of lath martensite in Ferrite-Martensite dual phase steel sheet annealed after cold-rolling, ISIJ Int. **55** (10) (2015) 2198–2205, https://doi.org/10.2355/isijinternational.ISIJINT-2014-641.

12. *K. A. Bello, S. B. Hassan, O. Aponbiede*, Effects of Austenitising Conditions on the Microstructures and Mechanical Properties of Martensitic Steel with Dual Matrix Structure, J. Min. Mater. Character. Eng. **11** (1) (2011) 69–83, doi: https://doi.org/10.4236/jmmce.2012.111006.

13. *O. Çavuşoğlu, S. Toros, H. Gürün, A. Güral*, Warm deformation and fracture behaviour of DP1000 advanced high strength steel, Ironmak. Steelmak. **45** (7) (2018) 618–625, doi: https://doi.org/10.1080/03019233.2017.1309168.

14. *K. Bandyopadhyay, S. K. Panda, P. Saha, V. H. Baltazar-Hernandez, Y. N. Zhou*, Microstructures and failure analyses of DP980 laser welded blanks in formability context, Mater. Sci. Eng. **652** (2016) 250–263, doi: https://doi.org/10.1016/j.msea.2015.11.091.

15. *I. Faridmehr, M. Hanim Osman, A. Bin Adnan, A. Farokhi Nejad, R. Hodjati, M. Amin Azimi*, Correlation between Engineering Stress-Strain and True Stress-Strain Curve, Am. J. Civ. Eng. Archit. **2** (2014) 53–59, doi: https://doi.org/10.12691/ajcea-2-1-6.

16. *A. Kiraz, C. Kubat, Y. Y. Özbek, O. Uygun, H. Eski*, A web-based virtual experiment in material science: Tensile test laboratory application, Acta Phys. Pol. **125** (2) (2014) 310–312, doi: https://doi.org/10.12693/APhysPolA.125.310.

17. *N. Saeidi, F. Ashrafizadeh, B. Niroumand*, Development of a new ultrafine grained dual phase steel and examination of the effect of grain size on tensile deformation behavior, Mater. Sci. Eng. **599** (2014) 145–149, doi: https://doi.org/10.1016/j.msea.2014.01.053.

18. *J. Kadkhodapour, B. Anbarlooie, H. Hosseini-Toudeshky, S. Schmauder*, Simulation of shear failure in dual phase steels using localization criteria and experimental observation, Comput. Mater. Sci. **94** (2014) 106–113, doi: https://doi.org/10.1016/j.commatsci.2014.02.046.

19. *C. Netrasiri, S. Suranuntchai*, Damage curve determination of dual phase steel based on gtn mode-l failure criteria, Int. J. Mech. Eng. Robot. Res. **5** (4) (2016) 268–271, doi: https://doi.org/10.18178/ijmerr.5.4.268-271.

20. *F. Ozturk, S. Toros, S. Kilic*, Effects of anisotropic yield func-

tions on prediction of forming limit diagrams of DP600 advanced high strength steel, Procedia Eng. **81** (2014) 760–765, doi: https://doi.org/10.1016/j.proeng.2014.10.073.

21. *G. Chen, M. F. Shi, T. Tyan*, Fracture Modeling of AHSS in Component Crush Tests, SAE Int. J. Mater. Manuf. **4** (2011) 1–9, doi: https://doi.org/10.4271/2011-01-0001.

22. *J. Marzbanrad, S. Norozi, A. Ahmadi*, Damage modeling in crashworthiness of dual-phase steel, Int. Conf. Mech. Eng. **21** (2013) 7–12, ISME 2013-1970.

23. *A. Ramazani, K. Mukherjee, H. Quade, U. Prahl, W. Bleck*, Correlation between 2D and 3D flow curve modelling of DP steels using a microstructure-based RVE approach, Mater. Sci. Eng. **560** (2013) 129–139, doi: https://doi.org/10.1016/j.msea.2012.09.046.

24. *M. Otroshi, M. Rossel, G. Meschut*, Stress state dependent damage modeling of self-pierce riveting process simulation using GISSMO damage model, J. Adv. Join. Process. **1** (2020) 100015, doi: https://doi.org/10.1016/j.jajp.2020.100015.

25. *A. Mathevon, D. Fabrègue, V. Massardier, S. Cazottes, P. Rocabois, M. Perez,* Investigation and mean-field modelling of microstructural mechanisms driving the tensile properties of dual-phase steels, Mater. Sci. Eng. **822** (2021) 141532, doi: https://doi.org/10.1016/j.msea.2021.141532.

26. *Y. Xiao, Y. Hu*, An extended iterative identification method for the GISSMO model, Metals (Basel). **9** (5) (2019) 568, doi: https://doi.org/10.3390/met9050568.

27. *W. Liu, J. Lian, S. Münstermann*, Damage mechanism analysis of a high-strength dual-phase steel sheet with optimized fracture samples for various stress states and loading rates, Eng. Fail. Anal. **106** (2019) 104138, 2019, doi: https://doi.org/10.1016/j.engfailanal.2019.08.004.

28. *R. Santos, L. Da Silveira, L. Moreira, M. Cardoso, F. Da Silva, A. Dos Santos Paula*, Damage identification parameters of dual-phase 600-800 steels based on experimental void analysis and finite element simulations, J. Mater. Res. Technol. **8** (1) (2019) 644–659, doi: https://doi.org/10.1016/j.jmrt.2018.04.017.

29. *B. Valoppi, S. Bruschi, A. Ghiotti, R. Shivpuri*, Johnson-Cook based criterion incorporating stress triaxiality and deviatoric effect for predicting elevated temperature ductility of titanium alloy sheets, Int. J. Mech. Sci. **123** (2017) 94–105, doi: https://doi.org/10.1016/j.ijmecsci.2017.02.005.

30. *H. Chalal, F. Abed-Meraim*, Determination of forming limit diagrams based on ductile damage models and necking criteria, Lat. Am. J. Solids Struct. **14** (10) (2017) 1872–1892, doi: https://doi.org/10.1590/1679-78253481.

31. *N. E. Karkalos, A. P. Markopoulos*, Determination of Johnson-Cook material model parameters by an optimization approach using the fireworks algorithm, Procedia Manuf. **22** (2018) 107–113, doi: https://doi.org/10.1016/j.promfg.2018.03.017.

32. *N. Specimen*, Effect of Stress Triaxiality on Plastic Damage Evolution and Failure Mode for 316L, Metals **9** (10) (2019) 1067, doi: https://doi.org/10.3390/met9101067.

33. *Z. Wang, Z. Hu, Z. Liu, G. Chen*, Application of a material model based on the Johnson-Cook and Gurson-Tvergaard-Needleman model in ship collision and grounding simulations, Ocean Eng. **205** (2020) 106768, doi: https://doi.org/10.1016/j.oceaneng.2019.106768.

34. *S. Toros, F. Ozturk*, Modeling uniaxial, temperature and strain rate dependent behavior of Al-Mg alloys, Comput. Mater. Sci. **49** (2) (2010) 333–339, doi: https://doi.org/10.1016/j.commatsci.2010.05.019.

35. *R. M. Caddell, W. F. Hosford*, Metal Forming: Mechanics and Metallurgy, 4th Ed., Cambridge University Press, 2011.

SAŽETAK
Mehaničko ponašanje dvofaznih čelika pri različitim brzinama naprezanja
Labinot Topilla i *Serkan Toros*

Cilj ovog istraživanja bio je analizirati deformiranje troaksijalnih uzoraka dvofaznih čelika DP600 i DP800 pri naprezanju. Mikrostruktura analiziranih čelika uglavnom sastoji od feritne i martenzitne faze. Ti čelici nalaze široku primjenu u automobilskoj industriji koja je u stalnoj potrazi za kvalitetnijim materijalima koji će dovesti do povećanja sigurnosti vozila, zaštite okoliša ili smanjenja potrošnje goriva. U ovom radu su za sve uzorke provedeni jednoosni vlačni testovi pri trima brzinama naprezanja: 0,0083, 0,042 i 0,16 s^{-1}, da bi se odredila mehanička svojstva ispitivanih čelika kao što su naprezanje, deformacija, granica elastičnosti i granica kidanja. Osim toga, metodom konačnih elemenata pomoću Mat_Picewise_Linear_Plasticity_024 modela simulirani su jednoosni vlačni testovi s karakteristikama sličnim eksperimentalnim. Rezultati numeričke simulacije uspoređeni su s eksperimentalnim rezultatima. Usporedba je napravljena pri granici kidanja, a prosječna točnost oba čelika za uzorke standarda (s) bila je < 1 %, za (20a) uzorke 1,50 %, za (4a) uzorke 4 % i za (a) uzorke 3,50 %, ukazujući na prikladnost modela.

Ključne riječi
Troosni, dvofazni čelik, numeričke simulacije, brzina deformacije, granica neuspjeha